Detailed microstructure and the influence of post-treatment on CVD TiAlN wear-resistant coatings

Citation for the original published paper (version of record):
Mead, M., Bäcke, O., Manns, T. et al (2025). Detailed microstructure and the influence of post-treatment on CVD TiAlN wear-resistant coatings. International Journal of Refractory Metals and Hard Materials, 129. http://dx.doi.org/10.1016/j.ijrmhm.2025.107077

International Journal of Refractory Metals and Hard Materials 129 (2025) 107077

Contents lists available at ScienceDirect

International Journal of Refractory Metals and Hard Materials

journal homepage: www.elsevier.com/locate/IJRMHM

Detailed microstructure and the influence of post-treatment on CVD TiAlN wear-resistant coatings

Monica Mead [a,*], Olof Bäcke [a], Thorsten Manns [b], Dirk Stiens [b], Mats Halvarsson [a]

[a] Department of Physics, Chalmers University of Technology, SE-412 96 Gothenburg, Sweden
[b] Walter AG, Derendinger Str. 53, 72072 Tübingen, Germany

ARTICLE INFO

Keywords:
TiAlN
LPCVD
STEM
TKD
growth mechanism
lattice distortion
slip system

ABSTRACT

In this work, the growth modes of low-pressure chemical vapour deposition (LP-CVD) nano-lamellar TiAlN coatings deposited on cemented carbide substrates and the influence of blasting post-treatment on the microstructure are investigated by scanning electron microscopy (SEM), scanning transmission electron microscopy (STEM) and transmission Kikuchi diffraction (TKD). Detailed information on the microstructure is revealed and gives insight into the growth mechanisms during deposition. Local information on the influence of blast-treatment on the micro- and nanostructure reveals how the material is influenced by external stresses on a microstructural level.

Two distinct surface morphologies corresponding to specific grain orientations with <111> and <110> directions parallel to the coating normal are observed. Additionally, a growth mechanism is proposed, which suggests that the surface reaction kinetics are influenced by the detailed microstructure of the grains, leading to locally varying Al/Ti ratios. Blast-treatment of the TiAlN coatings leads to bending and intermixing of the nano-lamellae, where the direct visualization of the lamellae enabled the estimation of the deformation. Continuous lattice rotations were observed in the near-surface region, where the magnitude of the lattice rotation in areas with a high orientation density of <110> directions was more pronounced as compared to areas with a high orientation density of <111> directions. This could be related to the local Schmid factors.

1. Introduction

During metal machining, cutting tools are subject to high temperatures and pressures. Therefore, both hardness and toughness of cutting tools are required to be high, for which reason mainly cemented carbides are used on the market [1,2]. Because failure at high temperatures mainly occurs at or close to the interface of the cutting tool surface and the workpiece, coatings are generally deposited on cutting tool materials to enable the independent tailoring of volume and surface properties [1,3]. Increasing demands create a trend towards even higher cutting temperatures where the role of failure due to diffusion and oxidation becomes critical [1,4]. Therefore, oxidation and corrosion resistance, as well as thermal resistance, are important properties of cutting tool coatings in addition to wear resistance, low friction coefficients, high fracture toughness and hardness.

Coatings of cubic TiAlN with rock salt (B1) crystal structure exhibit good chemical stability, oxidation resistance, hot hardness as well as a relatively low friction coefficient and wear rate [5–7]. In particular, the hardness, oxidation and corrosion resistance of TiAlN can be further improved by increasing the Al content [7,8]. While the Al content of cubic TiAlN coatings was previously limited to about 67 at.% (metal content) in coatings prepared by physical vapour deposition (PVD) [1,9,10], deposition by low-pressure chemical vapour deposition (LP-CVD) has enabled Al contents up to 90 at.% without the formation of significant amounts of undesirable hexagonal AlN, which impairs the mechanical properties [11–13]. In LP-CVD TiAlN coatings a nano-lamellar arrangement of Ti- and Al-rich regions growing epitaxially with a cube-on-cube relationship along the <100> directions is observed as a consequence of the kinetics of the chemical reactions during deposition [13–15]. The spacing of the nano-lamellae can be tuned by the speed of the rotational precursor gas supply, as shown by Qiu et al. [14]. The nano-lamellar arrangement might contribute to phase stabilisation of the cubic phase and with that a higher thermal stability of LP-CVD TiAlN coatings compared to those prepared by PVD

---

* Corresponding author.
E-mail addresses: monica.mead@imw.uni-stuttgart.de (M. Mead), obacke@chalmers.se (O. Bäcke), thorsten.manns@walter-tools.com (T. Manns), dirk.stiens@walter-tools.com (D. Stiens), mats.halvarsson@chalmers.se (M. Halvarsson).

https://doi.org/10.1016/j.ijrmhm.2025.107077
Received 15 October 2024; Received in revised form 24 January 2025; Accepted 24 January 2025

[15]. Furthermore, an influence on the mechanical properties such as the hardness and elastic modulus due to interfacial straining could be possible and dependent on the lamella periodicity [14]. Commonly, the LPCVD TiAlN coatings exhibit (111) texture [11,13,15], however (100), (110), (211) and (311) textures have also been reported [16–19]. It can be expected that the texture will also influence the mechanical properties [20–24]. Despite existing abundant research on the growth of TiAlN coatings by LP-CVD and the evolving micro- and nanostructure, a comprehensive understanding of the growth mechanisms and intricate microstructural characteristics is still lacking.

In addition to tuning the composition, crystal structure and microstructure by adapting the deposition to optimize the coating properties and resulting performance, post-treatment can be performed. Blasting of other cutting tool coatings, such as Al_2O_3, has proven the ability to transform coatings from residual tensile stress states to compressive stress [25–29]. This can lead to the closing of thermal cracks [28,29], as well as increasing coating hardness and decreasing surface roughness, resulting in better wear resistance and overall improved tool life [25,27,29,30]. Previous studies of blast-treatment on TiAlN coatings have shown an increased fracture toughness [31] and tool life, especially in the case of wet-blasting [32]. Although the positive effect of blast-treatment on the general stress state of wear-resistant coatings has received attention in several scientific studies, there remains a relative sparsity of research investigating its influence on the microstructure in the near-surface region and the local effects of blasting on the crystal lattice.

In this work TiAlN coatings deposited on cemented carbide substrates by LP-CVD are investigated by scanning electron microscopy (SEM), scanning transmission electron microscopy (STEM) and transmission Kikuchi diffraction (TKD) to reveal detailed information on the microstructure and give insight into the growth mechanisms. In particular, the observed surface morphologies are connected to grain growth modes, where surface kinetics, surface energies, texture and the development of facets play important roles. In addition, blast-treated coatings are characterised to acquire local information on the influence on the micro- and nanostructure. This reveals information on how the material is influenced by external stresses on a microstructural level, where possible influences of the varying nano-lamella periodicity, as well as the initial microstructure and texture, are considered.

2. Materials and methods

2.1. LPCVD synthesis

TiN/TiAlN/TiN multilayers were deposited in one deposition run on cemented carbide substrates of ISO 1832 SNMA 120404 and SPHW 120408 geometry with a composition of 95 wt% WC, 6 wt% Co and 90.6 wt% WC, 1.4 wt% other carbides, 8.0 wt% Co, respectively and an average WC grain size in the range of 0.5 μm – 1.0 μm. The geometries of the two substrates are very similar, showing largely flat surfaces without complicated convex or concave features such as chip breakers. Therefore, the gas flow conditions close to the substrate surface should be similar and the deposition and resulting coatings comparable.

A TiAlN layer of approximately 6 μm thickness was deposited using $AlCl_3$, $TiCl_4$, NH_3 and H_2 as precursor gases at a deposition temperature of 725 °C and a pressure below 25 mbar. Three different rotation speeds (0.5, 2 and 5 rpm) of the precursor gas beam enabled the deposition of TiAlN coatings with different lamella periodicities (as presented in the result section). TiN layers were deposited below and beneath the TiAlN layer in the same deposition run, first as an innermost base layer for the TiAlN layer, acting as a diffusion barrier and adhesion layer [1], and second as an outermost decor layer providing easy wear detection. For the deposition of the TiN layers $TiCl_4$, N_2 and H_2 were used as precursor and carrier gases at 850 °C and a pressure below 150 mbar. Further details of the LP-CVD synthesis are stated in [14,33].

2.2. Post-treatment: Blasting

The deposited coatings were subjected to wet-blasting at an angle of 90° to the sample surface (top-blasting) with an Al_2O_3 (corundum) grit and a pressure of 2.0 bar for 54 min. A mesh grit size of FEPA 230 was applied corresponding to a mean grit size of about 82 μm according to the FEPA (Federation of European Producers of Abrasives) standard. Further details are specified in [34].

Samples of the three different rotation speeds were investigated both before and after blasting.

2.3. Characterization methods

2.3.1. X-ray diffraction

For the determination of the coating phases, composition calculations according to Vegard's law and calculation of texture coefficients, X-ray diffraction (XRD) was performed using a Panalytical Empyrean Diffractometer with Cu Kα-radiation run at 40 kV and 40 mA with a PIXcel 1D detector. In the incident beam path, Soller slits with 0.04 rad divergence, a fixed incident beam mask with 5 mm width, a 0.5° divergence slit, and a 1° anti-scatter slit were used. In the diffracted beam path, a Ni Kβ filter, Soller slits with 0.04 rad divergence and a 4° anti-scatter slit were used. Symmetrical θ-2θ-scans were performed within the angle range $28^\circ \le 2\theta \le 70^\circ$ with 0.026° step size. For the calculation of texture coefficients, measured peak area intensities were corrected for thin film thickness and absorption and referenced to modelled area intensities of a pattern calculated for $Ti_{0.25}Al_{0.75}N$ using the PowderCell software (presented in section A.2 in the supplementary material). Details are given in Table A1 of the supplementary material. The Al content was determined according to Vegard's law (Eq. A1 in the supplementary material) with $a = 4.24173$ Å for cubic TiN (PDF 00.038–1420 [35]) and $a = 4.04050$ Å for cubic AlN (PDF 01–077-6808 [35]) using the lattice parameter determined from the peak positions in the experimental data.

2.3.2. Scanning electron microscopy

Scanning electron microscopy (SEM) was performed using a Zeiss LEO Ultra 55 FEG for plan-view imaging of the rake face of as-deposited and blast-treated coated inserts. Secondary electrons (SE) were detected using an in-lens detector at an acceleration voltage of 3 kV and a working distance of 1–3 mm. Backscattered electrons (BSE) were detected at an acceleration voltage of 15 kV and a working distance of about 9 mm. Energy-dispersive X-ray Spectroscopy (EDX) was performed in a TESCAN Gaia3 FIB-SEM (focused ion beam-SEM) at an acceleration voltage of 20 kV and a working distance of about 10 mm. The Oxford Instruments Aztec software was used for the evaluation of the acquired spectra.

2.3.3. Scanning transmission electron microscopy

For imaging by scanning transmission electron microscopy (STEM) an FEI Titan 80–300 TEM/STEM was operated at 300 kV acceleration voltage in STEM mode. Thin-foil cross-sectional specimens of the coatings from different positions on the inserts attached to a Cu-grid were prepared by the lift-out technique with the FIB-SEM. Using a TEM double-tilt holder allowed tilting to a suitable zone axis (<110> or <100>) of an individual grain to image the Ti- and Al-rich lamellae. STEM brightfield (BF) and high-angle annular dark field (HAADF) images were recorded. EDX spectra were recorded within specific areas and evaluated within the TEM imaging & analysis (TIA) software by Thermo Fisher Scientific.

2.3.4. Transmission Kikuchi diffraction

The cross-sectional thin-foil lift-outs were also characterised by transmission Kikuchi diffraction (TKD) in a TESCAN Gaia3 FIB-SEM equipped with an electron backscatter diffraction (EBSD) detector at an acceleration voltage of 15 kV and a step size of 20–50 nm. Kikuchi lines were detected and processed by the Oxford Instruments Aztec software, which provides indexing based on comparison with a theoretically calculated electron backscatter pattern of the expected crystal structure. For this, data was retrieved from the Materials Project for Ti3AlN (mp-10675) from database version v2023.11.1 [36]. Data analysis, Schmid factors calculation and plotting were performed using the free Matlab toolbox MTEX [37]. The grain orientation spread (GOS), grain reference orientation deviation (GROD) and orientation distribution function (ODF) were determined based on the unfiltered data. Here, the GOS is the average misorientation angle from the grain's mean orientation, GROD is the misorientation compared to the mean orientation of its grain for each measured location (pixel) and the ODF associates each orientation with the volume percentage of grains with the same orientation, giving a quantitative description of the texture in units of multiples of uniform pole density (MUD). For the visualization of some data, the half-quadratic filter was applied to denoise (additive Gaussian noise) and fill missing data. The filter considers the next neighbours of each pixel and attempts to restore the original image by minimizing an energy functional [38].

3. Results

3.1. Crystal structure, nanostructure and texture

Investigations by XRD after deposition of the TiAlN coatings by LP-CVD showed Al contents above 80 at. % (listed in Table 1). Symmetrical XRD Bragg scans taken on the flank sides of the as deposited samples show virtually no signal from hexagonal AlN. The diffractograms and peak assignments are shown in Fig. A1 of the supplementary material. This is in good agreement with the observations from electron microscopy presented below which also indicate that the coating has cubic phase and only negligible amounts of hexagonal AlN, if any. The calculated texture coefficients of the different samples are also given in Table 1 using intensities of the (111), (200) and (220) reflections of the cubic TiAlN phase. They show preferred crystal orientation for (111) and (220), while the texture coefficient of (200) is low. In contrast to the electron microscopy-based analyses presented below, the XRD signal stems from the coating on the entire flank face of the insert. Additionally, the lamella spacing of the samples was determined from STEM HAADF images of the cross-sectional lift outs (examples are in Fig. 1) and is presented in Table 1. As expected, the largest periodicity is present in the sample deposited using the lowest rotational speed and the smallest periodicity in the sample deposited at the fastest rotational speed. The nominal lamella periodicity was determined according to Eq. B1 of the supplementary material. The expected lamella periodicities are 44.7 nm, 8.5 nm and 4.3 nm for the low, mid and high rotational speeds, respectively. The nominal values fit reasonably well with the experimentally measured periodicities, especially considering that thickness variations and possible inclination of the [111] direction to the sample normal [14] were not considered in this calculation.

Table 1
Experimentally determined Al content, peak area of hexagonal AlN, texture coefficients and lamella periodicity for the samples deposited at three rotation speeds (0.5, 2 and 5 rpm).

Sample	0.5 rpm	2 rpm	5 rpm
Al content [at.%]	82.9	85.4	81.2
Texture coefficient (111)	1.5	1.9	1.1
Texture coefficient (220)	1.2	0.8	1.8
Texture coefficient (200)	0.3	0.3	0.1
Average lamella periodicity [nm]	48 ± 9	6.8 ± 0.6	4.9 ± 0.4

3.2. Surface morphology and grain characteristics in as-deposited samples

Two distinct surface morphologies of the as-deposited samples could be distinguished. Firstly, the previously reported pyramidal surface morphology [14] and secondly, a ridge-like surface morphology, which are both shown in Fig. 2. Moreover, both occurred with relatively sharp edges (Fig. 2 (a) and (b)), as well as truncated (Fig. 2 (c) and (d)), where small pyramids or ridges were found on top of an additional surface roughly parallel to the sample surface. As the TiAlN coating is covered by a thin decor layer of TiN, it is unclear from the top-view SEM images whether the small pyramids or ridges on the truncated grains are a result of TiAlN or TiN growth. However, STEM HAADF images shown in Fig. 3 illustrate that the truncated TiAlN grains exhibit an additional core region (Fig. 3 (b)) compared to sharp-edged TiAlN grains (Fig. 3 (a)), where the nano-lamellae have a different orientation compared to the side regions. On a side note, Fig. 3 (a) was strictly speaking taken from a blasted sample. However, this feature should not be changed by blasting.

A closer look at the interface of the TiAlN and TiN layer in the core region of the truncated grain shows small steps of the TiAlN grain (Fig. 3 (c)) that are amplified in the top TiN layer, which exhibits even larger steps or even small facets (Fig. 3 (d)) that can be connected to the observations in the plan-view SEM images in Fig. 2. In addition, Fig. 3 (b) shows that the width of the core region increases along the growth direction of the grain. EDX spectra acquired from areas within the core or side regions of truncated grains in different samples show that the average Al content (considering only metal constituents) in the core region is higher than in the side regions, typically by about 5 at.%. Here, quantification was performed only regarding Ti and Al peak contributions as the deconvolution of the Ti and N peaks is challenging. Al contents of 84.5 at.% to 89.7 at.% were measured in the core region compared to 80.5 at.% to 84.2 at.% on the sides. The EDX measurements were not only performed on as-deposited samples, but also on blast-treated samples. In both cases the same trend is observed, indicating that, as expected, blasting does not influence this observation and instead these measurements provide improved statistics The individual data is presented in Table B1 in the supplementary material.

3.3. Microstructure of the surface region after blasting

3.3.1. Surface morphology after blasting

Compared to the surface morphologies of as-deposited samples presented in Fig. 2, the surface of blast-treated samples showed a relatively smooth surface. However, even after blasting it was in many cases possible to distinguish the previously pyramidal and ridge-like morphologies, owing to the remnants of the top TiN layer. This is shown in Fig. 4 where the contrast in Fig. 4 (a) shows triangular shapes and elongated shapes associated with the ridge-shaped grain morphology in Fig. 4 (b). The areas appearing brighter in Fig. 4 indicate a substantially higher Ti content (higher atomic number than Al and therefore increased backscattering coefficient) and are therefore considered to be remnants of the top TiN layer in the valleys of the pyramids or ridges. The higher Ti content in the brighter areas is additionally confirmed by EDX measurements of the sample surface (about 22 at. % Ti in the bright areas compared to 12 at. % Ti in darker areas considering only metal contents).

The remaining TiN also gives an indication of the amount of material removed by blasting. The deposited TiN layer has a thickness of around 0.5 μm, taking into account the surface roughness of the TiAlN layer, it can be approximated that about 0.5–0.8 μm of the multilayer coating was removed. This is also illustrated in Fig. B2 in the supporting information by overview images of the cross-sectional lift-outs. The present depth of coating removal is in a range that does not destroy the protective nature of the coating, as the TiAlN layer remains after blasting and the substrate is not revealed.

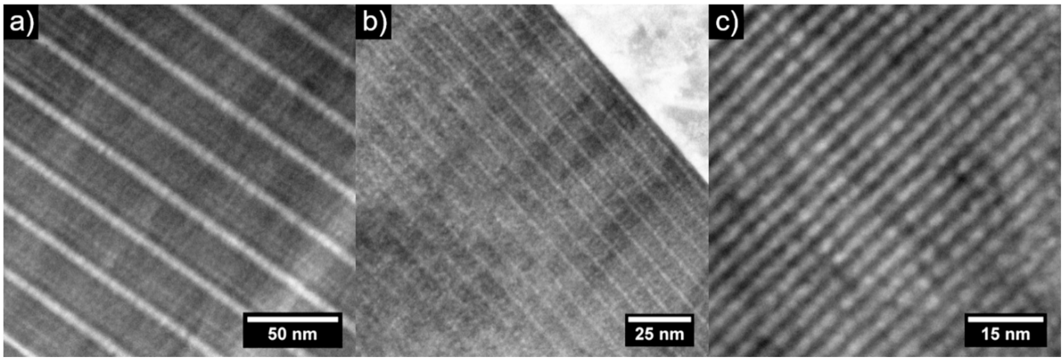

Fig. 1. STEM HAADF images of the cross-sectional lift-outs showing the observed lamellae of different spacing at (a) low rotation speed (0.5 rpm), (b) medium rotation speed (2 rpm) and (c) highest rotation speed (5 rpm).

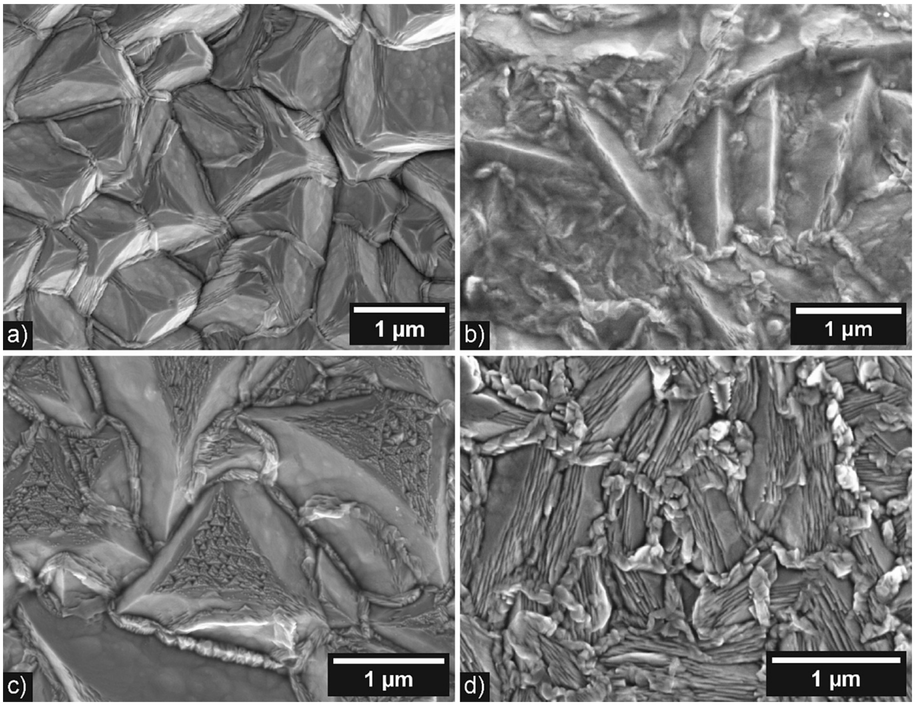

Fig. 2. Surface morphologies observed by plan-view SE imaging by SEM. (a) Pyramidal morphology (b) Ridge-like morphology (c) Truncated pyramidal morphology (d) Truncated ridge-like morphology.

3.3.2. *Near-surface region after blasting*

In STEM BF images of the cross-sectional lift-outs of the blasted samples, lattice rotations and an increased defect density in the near-surface region are observed by varying diffraction contrast, as illustrated in Fig. 5 (a). Quantification of the depth of the affected region near the surface is difficult and somewhat subjective, even more so as the contrast varies with changing angle of the thin-foil sample to the electron beam. However, a depth of a few hundred nanometres can be estimated, as indicated in Fig. 5 (a). The depth of the affected region was estimated from STEM BF images of the blast-treated samples for all three rotation speeds, where all had grain orientations primarily along the (111) orientation, as determined by TKD to exclude an influence of the grain orientation on the behaviour upon blasting. The corresponding images and measured depths can be found in Fig. B3 and Table B2 of the supplementary material. However, no clear influence of the rotation speed, and therefore lamella spacing, on the depth of the affected near-surface region could be identified.

Furthermore, Fig. 5 (b) illustrates that continuous lattice rotations in the near-surface region are introduced by blasting. In Fig. 5 (b) fast Fourier transformations (FFTs) from the corresponding regions in the STEM BF images show the orientation along the $[1\overline{1}0]$ zone axis and how the lattice rotates continuously within one grain. Within this small selected region of roughly 80 nm length, a lattice rotation of about 7° is observed.

When aligning individual grains to a zone axis orthogonal to their $\{100\}$ planes, the behaviour of the alternating Ti- and Al-rich lamellae can be observed. Fig. 5 (c) shows an example of lamellae bending in the near-surface region as a result of blasting. This was observed for samples prepared at all three rotational speeds (Fig. B4 in the supplementary material). In regions where the lamellae have moved from their original place, some mixing between the Ti- and Al-rich regions and changes in lamella spacing can be observed. In addition to bent lamellae, the disappearance of lamellae in the rotated lattice is observed, as shown in Fig. 5 (d). In the bottom right corner of Fig. 5 (d) lamellae are visible (though not as pronounced as in many other cases), however, they disappear in the region closer to the coating surface (top left area of the image) as marked by the blue line. Because this could also be explained by a projection effect due to the lattice rotations induced by blasting, the

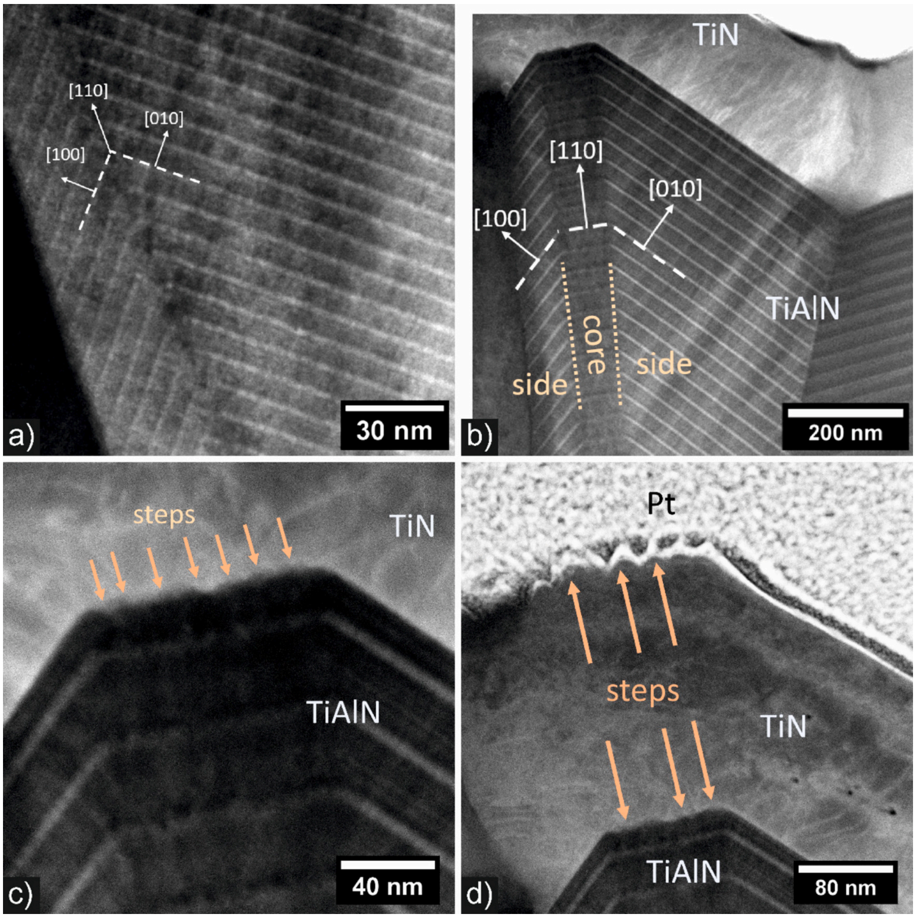

Fig. 3. STEM HAADF image of the cross-section of (a) a sharp-edged TiAlN grain, (b) a truncated TiAlN grain, (c) the top region of the truncated TiAlN grain at the surface of the core region, (d) the top TiN layer on the truncated TiAlN grain.

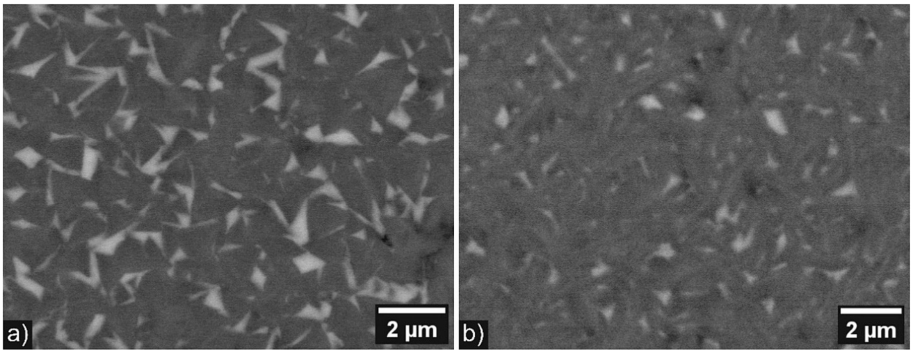

Fig. 4. SEM BSE plan-view images of blasted samples showing indications for (a) pyramidal morphology and (b) ridge-like morphology prior to blasting.

specimen was tilted according to the lattice rotation to ensure alignment along the zone axis even in the rotated near-surface area. However, despite these adjustments, no lamellae could be observed indicating intermixing of the Ti- and Al-rich regions in the near-surface region. Figures illustrating this are given in Fig. B5 of the supplementary material.

3.4. *Crystal orientations revealed by TKD*

3.4.1. *Crystal orientations and surface morphology*

To connect the previously presented surface morphologies (Fig. 2 and Fig. 4) to the local textures, cross-sectional lift-outs from corresponding regions were characterised by TKD from the blasted samples of all orientation speeds. Exemplary inverse pole figure (IPF) orientation maps at each position, as well as the IPF maps of the resulting ODF, are shown in Fig. 6. In line with what has previously been reported by Qiu et al. [14], the orientation density in the <111> direction is increased in comparison to a uniform density where the specimen was taken from a region with previously (before blasting) pyramidal surface morphology (Fig. 6 (c)). For specimens that were taken from a region with previously ridge-like morphology, an increased orientation density is observed in the <110> direction (Fig. 6 (d)). The observation of these two preferred orientations corresponds to the previously presented texture coefficients determined by XRD (Table 1), which also indicate that the growth orientation of the coatings has contributions both along {111} and {110}.

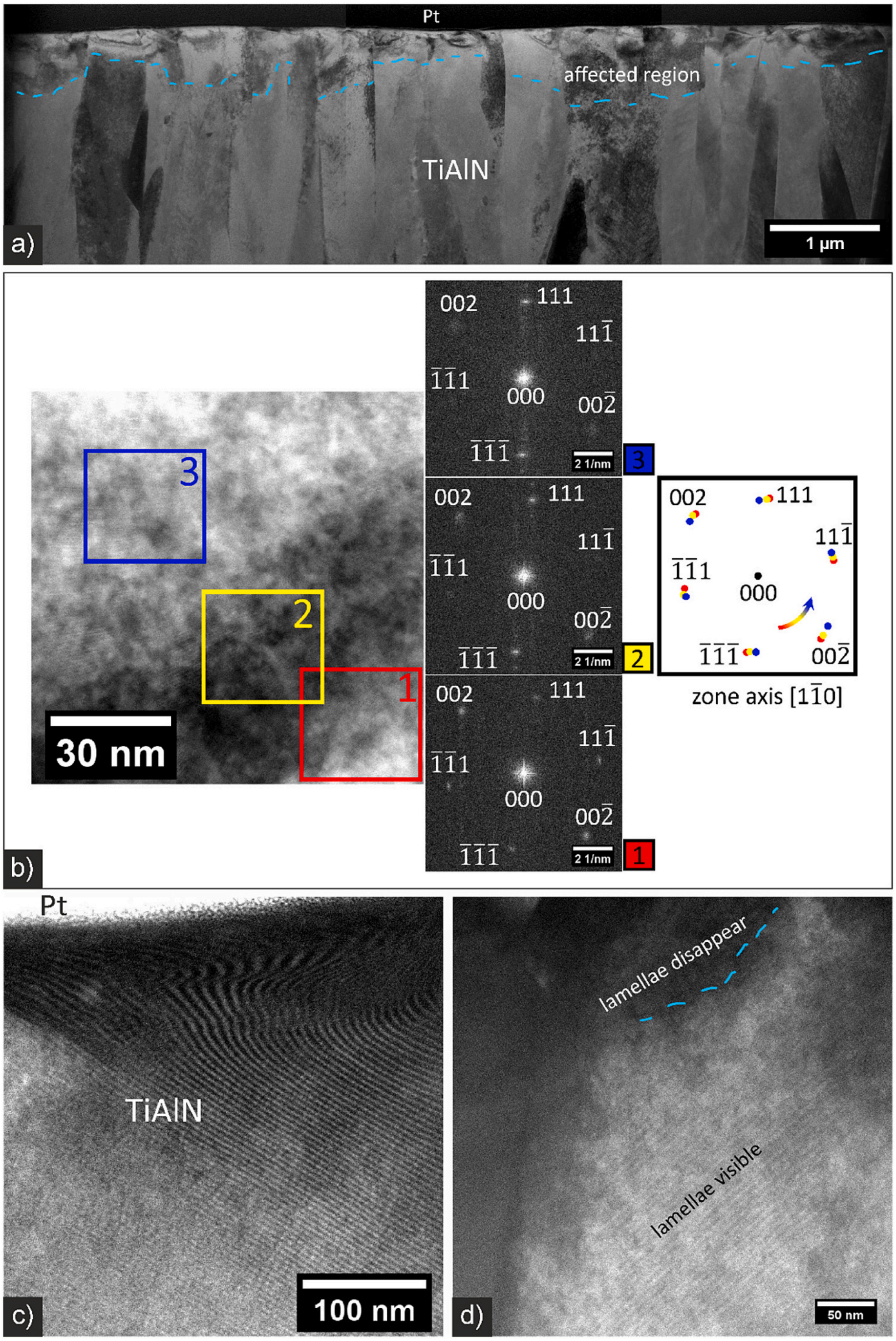

Fig. 5. Effects of blasting on the near-surface region of the TiAlN coating. (a) STEM BF image showing lattice rotations and an increased defect density (varying grain contrast in the near-surface region, above the dashed line). (b) Visualization of the lattice rotation by FFTs of the area of a grain shown in the STEM BF image on the left. The specimen was rotated to the zone axis in the areas marked by 1, 2 and 3. In addition to the rotation of the specimen to be at $[1\bar{1}0]$ zone axis, there is rotation around the zone axis, which is visualized by comparing the three FFTs. (c) Direct visualization of bending lamellae in the STEM HAADF image. (d) STEM HAADF image of disappearing lamellae in the near-surface region of a single grain.

3.4.2. Lattice rotations after blasting

The crystal orientations obtained by TKD were analysed further to retain information about the effects of the blast-treatment. Fig. 7 (a) shows the GOS of the grains after blast-treatment. Here, the GOS of those grains that reach the coating surface region (~ up to 1 µm) is systematically higher compared to the grains further down in the coating (left in Fig. 6 (a), vindicating that plastic deformation in the form of lattice rotations is introduced by blasting and affecting mainly the uppermost region of the coating. Fig. 7 (b) shows the continuous nature of the lattice rotations. A single grain is selected and the orientation of each pixel along the colour coded line is shown in the IPF. A continuous change of orientation in all three dimensions (X, Y and Z) is observed. The rotation is around 6.4° for the line distance of 1.6 µm, giving a lattice rotation of 4°/µm.

The lattice rotations are also evident in the GRODs in Fig. 8, where a higher density of high misorientation angles close to the coating surface (~0.5 µm) is evident. Typically, when presenting TKD or EBSD data it has undergone filtering to remove noise and missing data has been filled according to an algorithm of choice. In this case, this was specifically not done as the crystal orientations in the near-surface region change

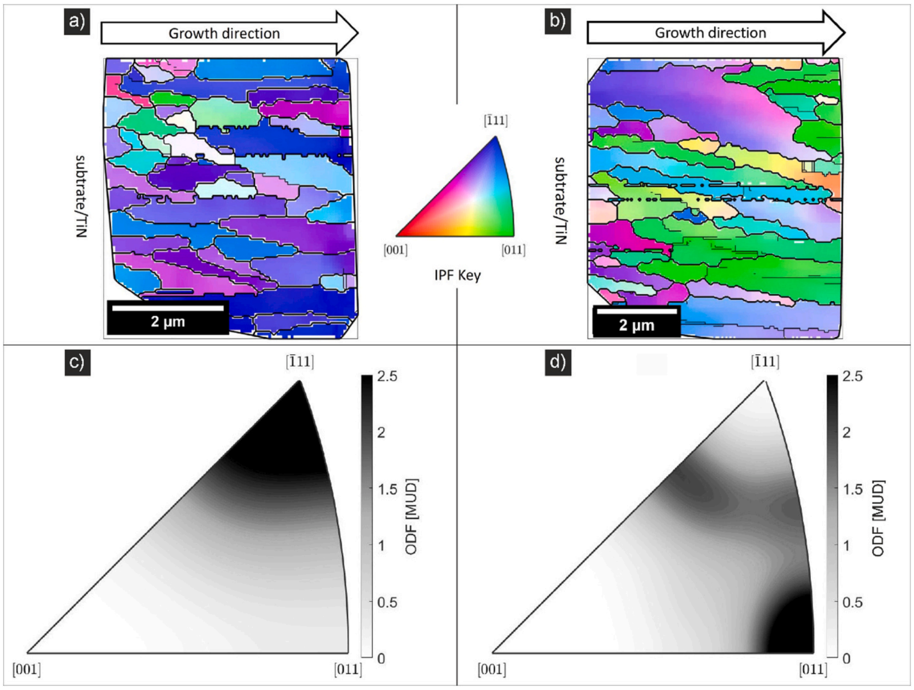

Fig. 6. Crystal orientations retrieved by TKD. IPF orientation maps of specimens from positions with (a) previously pyramidal and (b) previously ridge-like surface morphologies. Resulting ODFs are presented for the respective positions in (c) and (d). The corresponding lift-outs were obtained from a sample deposited at the intermediate rotation speed.

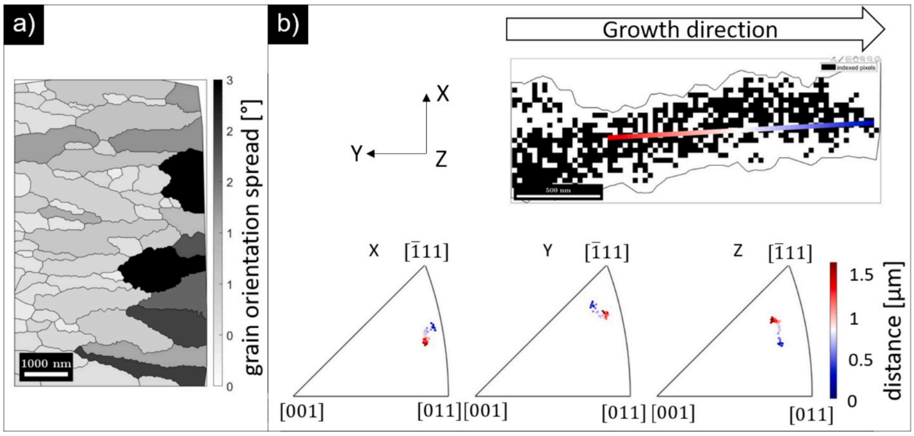

Fig. 7. Crystal rotations after blasting measured by TKD. (a) GOS (b) Data of a single grain from which the lattice orientation along the colour coded line was determined. The lattice rotation in three dimensions is illustrated in IPFs from the red (distance from coating surface = 0 µm) to the blue end (distance from coating surface = 1.6 µm). (For interpretation of the references to colour in this figure legend, the reader is referred to the web version of this article.)

substantially locally. Further, the amount of indexed data decreases significantly towards the top of the coating, in which case a lot of missing data would be interpolated based on only little experimental data. A closer look at the GRODs of regions with different prevalent orientations unveils a dependence on the crystal orientation. Fig. 8 shows the ODFs and GRODs of two specimens from different positions of the sample deposited at the medium rotation speed. In Fig. 8 (a) the ODF shows a preferred orientation in <111> direction (along the surface normal), while Fig. 8 (b) shows a preferred orientation in <110> direction. The corresponding IPF maps, as well as further examples, can be found in section C of the supplementary material. Comparing the scale bars of the two GROD maps, the maximum value is generally higher for the <110> than the <111> textured specimens by about 3°; 6–7° compared to 3–4° misorientation. This shows that there is a more pronounced lattice rotation as a result of blast-treatment in regions with preferred orientation in <110> orientations compared to regions with preferred <111> orientations.

4. Discussion

4.1. Surface morphology and connection to growth mode

4.1.1. Connecting the surface morphology and the growth direction

In previous publications, the observation of a pyramidal surface morphology of similar TiAlN coatings with a (111) texture has been explained by competitive growth. The growth of (111) oriented pyramidal grains is the result of a high surface energy of {111} planes, while {100} planes have a low surface energy, and therefore form the surfaces of a pyramid [14]. The high growth rate of these grains compared to randomly oriented grains leads to the evolution of a (111) texture of the

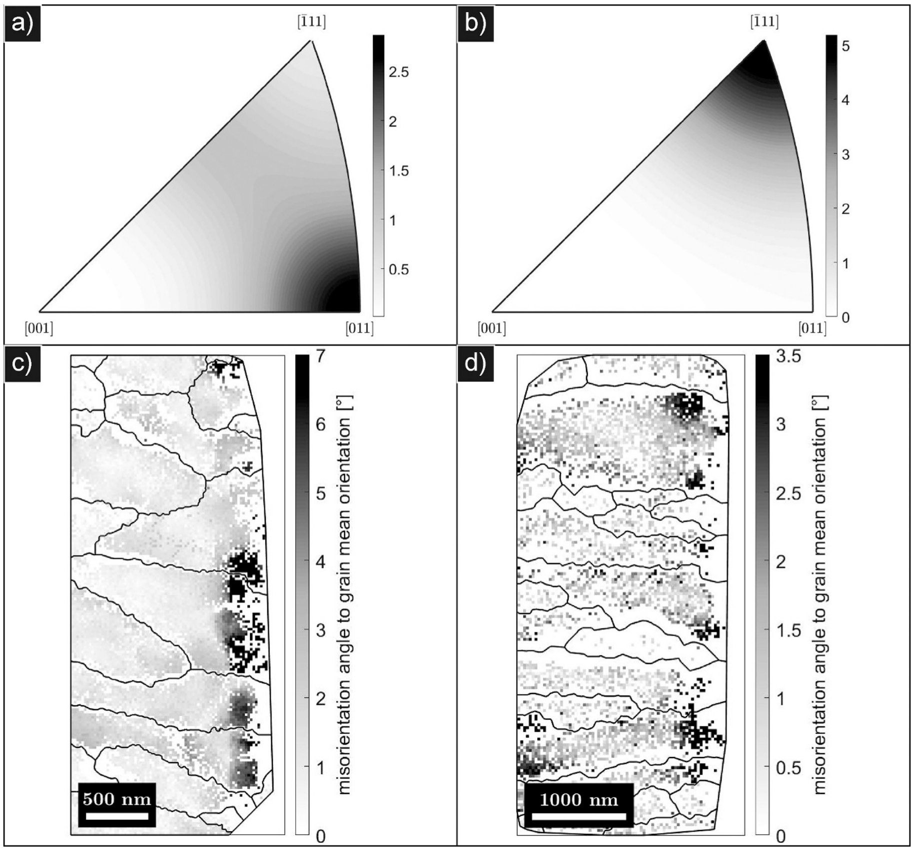

Fig. 8. ODFs and GRODs of a specimen from positions with preferred orientation in (a), (c) the <110> direction, and (b), (d) the <111> direction.

coating. The connection between <111> oriented grains and pyramidal grain morphology is supported also by the present work (Fig. 6 (c)). Additionally, a ridge-like morphology is observed and connected to grains with a preferred orientation along <110>. Therefore, the surface morphology can give an indication of the local texture of the coating. However, the previously reported (110) textured TiAlN coatings did not exhibit a ridge-like surface morphology [17].

Generally, there are three different possibilities for the grain growth direction that will lead to grains with low-energy {100} facets. They are illustrated in Fig. 9. Firstly, growth along a <100> direction, which would result in flat {100} surfaces making up a cube or rectangular prism shaped grain (cuboid). This is not observed in the present case, as evidenced by the low (200) texture coefficient determined by XRD. The other two possibilities are the observed growth in <110> and <111> directions. Both of these orientations should be kinetically preferred during competitive growth of randomly oriented grains (no epitaxy) in a polycrystalline film [39]. However, a slightly inclined growth can also lead to a deviating overall texture, such as (211) formed by tilted (111) oriented grains [18].

4.1.2. Growth of truncated grains

Considering surface energies, the formation of an additional surface on top of the two differently oriented truncated grains seems highly unlikely if it were a facet of a high-energy {111} or {110} plane. This geometric consideration is illustrated in Fig. 10 (a). The differently oriented lamellae in the core region compared to the side regions seem to indicate a corresponding growth of a {111} or {110} plane in the core regions (Fig. 3). However, it was established in Section 3.2 that the additional surface of the truncated TiAlN grains is stepped (Fig. 3). Thus, they do not show {111} or {110} facets, instead the small steps seem to consist of {100} facets. Therefore, the grains do not exhibit any high energy facets, as illustrated in Fig. 10 (b). These steps of the top surface

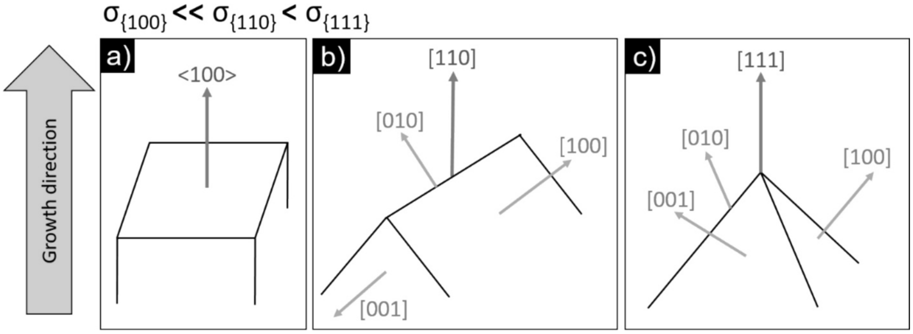

Fig. 9. Three possibilities of grain growth with {100} surfaces with low energy $\sigma_{\{100\}}$. (a) Flat {100} surfaces parallel and perpendicular to the growth direction. (b) Ridge-like surface morphology with an overall growth along <110>. (c) Pyramidal grains with an overall growth along <111>.

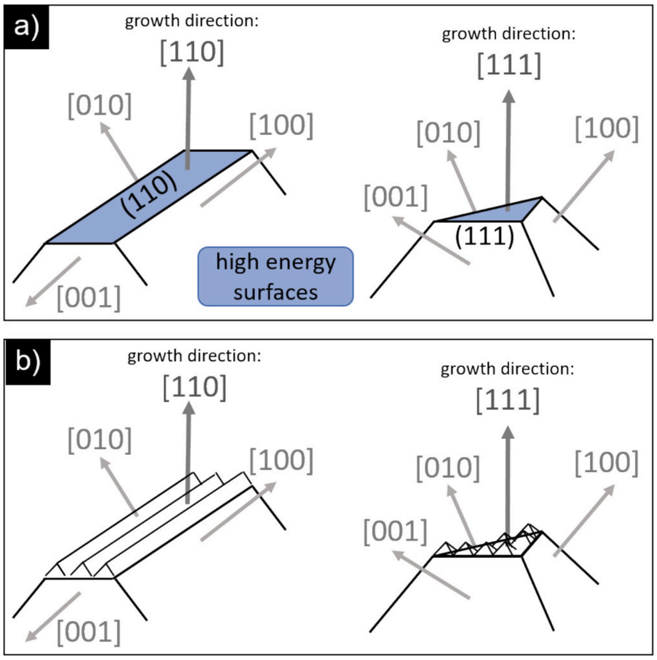

Fig. 10. Geometrical considerations of truncated grains. a) If the top surface of truncated grains were facets, they would consist of high energy {110} or {111} surfaces. b) In the observed case the top surface of truncated grains is stepped and therefore still shows small {110} facets. Therefore, the truncated grains do not exhibit high energy facets.

of the grains also explain the more smeared out appearance of lamellae in the core region compared to the side regions that are observed in STEM images by projection effects (Fig. 3). The outer TiN decor layer replicates and even amplifies these small steps, also exhibiting {100} facets, as it also (just like TiAlN) has a low (100) surface energy [40].

On the stepped surface many ledges and kinks are present, where both adsorption and dissociation of precursor molecules are preferred during deposition due to lower energy. This influences the nucleation behaviour and increases the adsorption and dissociation rate [41]. Special sites like this also exist on the side {100} facets, yet, the density is substantially increased on the stepped surface, decreasing the diffusion paths to reach these special sites. Generally, during CVD adsorption, dissociation and surface diffusion of the reactive precursor gas molecules are the processes that influence the kinetics of the surface reactions.

Consequently, the surface reaction kinetics on the stepped top surface are enhanced compared to the flat side facets. Ti deposition from $TiCl_4$ at moderate temperatures, such as in the present case, is considered to be limited by mass transport (main gas flow and transport to the surface through a boundary layer) [11]. Therefore, Ti deposition is not strongly influenced by the increased surface reaction kinetics on the stepped top surface, as the surface reaction even on the flat side facets is still faster than the rate of arrival of precursor to the surface.

In contrast, Al deposition is reported to be limited by the surface kinetics in the present conditions [11]. Thus, the Al deposition on the stepped top surface with its higher surface reaction rates is enhanced compared to the flat side facets. This asymmetry in deposition rate for Al on the stepped top surface compared to the flatter side facets is therefore assumed to lead to the observed increase in Al/Ti ratio in the core region of a truncated grain compared to the side regions Fig. 11. Thermodynamically, fast-growing surfaces with high energy disappear to achieve the Wulff shape [41], as is also the case for the sharp pyramids and ridges in the present work. However, the formation of more facetted grain shapes compared to the thermodynamically favoured Wulff shape is typical during thin film deposition for kinetic reasons. The truncated grains observed in this work are evidence of this. In truncated grains, the width of the core region, and thus the area of the stepped surface which on the micrometre scale is a high energy surface, increases with grain height (contrary to what would be expected thermodynamically) Fig. 3 (b). On a nanometre scale, it becomes clear that small low energy {100} surfaces are formed, which can facilitate an increased lateral growth rate of the core regions, contributing to the kinetic stability of this growth mode and preserving the truncated morphology of the grains.

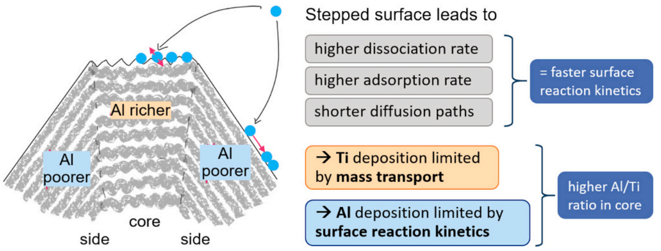

Fig. 11. Illustration explaining the increased Al deposition in the core region of a truncated grain. The dissociation and adsorption rate are increased at special sites such as kinks and steps. On the stepped surface the diffusion paths to such a special site are decreased compared to the flat facets on the sides.

4.2. *Effect of blast-treatment*

The plastic deformation observed indicates that the blast-treatment is suitable to change the stress state of the coating, and doesn't simply remove material. Though, this occurs mainly in the near-surface region, whereas further down towards the substrate the coating is not influenced as markedly. A gradient of induced compressive stress as a result of blast-treatment has been reported previously [26]. The observed plastic deformation is in contrast to previous observations by Barbatti et al. who did not observe any plastic deformation in CVD κ-Al_2O_3 coatings [42]. However, the mechanical response of the two materials should be different, as κ-Al_2O_3 is orthorhombic and not cubic as TiAlN is. In addition to the data that shows clear lattice rotation of the near-surface region of the coating (Fig. 7), the worsening indexing of the TKD data (Fig. 7 (b)) also indicates an increased defect density, introducing disorder and disturbance of the lattice periodicity and therefore leading to less clear Kikuchi bands that the analysis software has trouble with detecting and indexing.

The unique opportunity to track deformation with the help of direct visualization of the deformed lamellae (Fig. 5) also enables a quantitative estimation of the induced strain. The procedure, given in the supplementary material [43], results in an estimated substantial compressive strain of up to 2.6. In addition to the trackable bent lamellae, intermixing of the Ti- and Al-rich regions was observed (Fig. 5 (b) and (c)). Similar observations of regions where layers of TiAlN and CrN intermixed and distorted as a result of wear tests have been published [44]. In that work, the intermixing is attributed to a local increase in temperature that facilitated activation of diffusion in addition to plastic deformation. In the case of TiAlN, an increase in temperature (heating without blasting) would likely lead to spinodal decomposition of the metastable TiAlN phase [45,46]. Therefore, the intermixing in the present case is assumed to more likely be a result of plastic deformation instead of increased temperatures during blasting. Consequently, it would be a more severe case of the examples where distortion and only slight intermixing is observed. Of course, not only the magnitude of the blasting-induced strain, but also the direction of the plastic deformation in relation to the direction of the lamellae influence the degree of lattice bending and intermixing.

The observation of a more pronounced lattice rotation as a result of blast-treatment in regions with preferred <110> orientations compared to regions with preferred <111> orientations is in line with previous studies, where an increased hardness for (111)-oriented fcc TiAlN (and fcc TiN) compared to (100) or (110) orientations has been observed [47–49]. The experimental results can be used to indicate the activated slip systems for TiAlN during wet-blasting. Generally, they are currently unknown for TiAlN and depend both on the Al and N concentrations and the temperature. The probable slip systems for the rock salt structure are $\{111\} < 1\overline{1}0 >$, $\{110\} < 1\overline{1}0 >$ and $\{001\} < 110 >$ (the <110> directions are close-packed). For TiN, the main slip systems have been theoretically and experimentally determined to be $\{111\} < 1\overline{1}0 >$ and $\{110\} < 1\overline{1}0 >$ at room temperature and elevated temperature [50]. The Schmid factors for these slip systems are lower for a force in the [111] direction compared to a force in the [110] direction (illustrated in Fig. E1 in the supplementary information). Only for the $\{001\} < 110 >$ slip system is the Schmid factor higher for a force in [111] direction compared to a force in [110] direction. In this work, the experimentally observed lattice rotation is less for the (111) textured regions compared to the (110) textured regions, indicating a lower Schmid factor of the active slip systems for a force in <111> directions than for <110>. This leads to the conclusion that – analogously to TiN - mainly the $\{111\} < 1\overline{1}0 >$ and/or $\{110\} < 1\overline{1}0 >$ slip systems are activated at the relatively low temperatures during wet-blasting of the present TiAlN coatings with Al contents of 80–85 % metal content.

The microstructure of the studied LP-CVD TiAlN coatings and the effects of blast-treatment may have implications on the cutting performance. As initially introduced, (wet-)blasting has been reported to transform coatings from a state of residual tensile stress to residual compressive stress, creating a stress profile in the coating to a depth up to 1.5 μm [25–29]. This fits well with the lattice rotation's depth of a few hundreds of nanometres observed in the cross-sections of the blast-treated TiAlN coatings in this work. Blasting post-treatment has further been shown to increase coating hardness as well as fracture toughness and decrease surface roughness, which can positively influence other relevant properties, such as the friction coefficient and adhesion, which can lead to better wear resistance and overall improved tool life [25,27,29,30,42]. The applied blasting protocol has shown to increase the average tool lifetime by a factor of 2.8 compared to non-post-treated $Ti_{1-x}Al_xC_yN_z$ coatings in milling of stainless steel [34]. Whether this is due to the introduction of compressive stress, lattice rotations, reduction of surface roughness or other factors is unclear. However, Zhong et al. [29] have compared the influence of different post-treatments on the tool performance in turning of grey cast iron, and have found that blasting has a larger impact on tool life compared to only polishing. Among the effects of blasting, the change of surface roughness thus has a less pronounced effect on tool life than the stress state and resulting change in mechanical properties.

5. Conclusions

This work presents the detailed microstructure of TiAlN coatings prepared by LP-CVD. The coatings have high Al contents (80–85 at.%, metal content) without the formation of significant amounts of hexagonal AlN. Three lamella spacings are achieved by varying the rotational speed of the precursor gas supply and the experimentally determined periodicities correspond well with the theoretically calculated values. By combining the study of the microstructure by top-view SEM imaging with TKD measurements of lift-outs from regions with distinct surface morphologies, the connection between a pyramidal morphology and growth along a <111> direction is identified. Additionally, a ridge-like morphology is assigned to growth along a <110> direction. Both growth directions enable fast grain growth with low energy {100} facets, which explains the observed textures by the concept of competitive growth [39].

Furthermore, both observed morphologies (pyramidal and ridge-like) are observed in a truncated variation, where a stepped surface perpendicular to the growth direction appeared. Truncated grains show an additional core region in which the Al content is higher compared to the side regions (by about 5 at.%). This variation in Al content is explained by increased surface reaction kinetics on the stepped surface of the core region, leading to an increased deposition rate of Al there, while the Ti deposition is less influenced by surface conditions, and instead mainly limited by mass transport in the applied deposition conditions.

The effects of blast-treatment on the detailed microstructure and lattice orientation are also studied. Both bending and intermixing of the nano-lamellae are observed, where the direct visualization of the lamellae provides a unique opportunity to track and estimate the degree of deformation. A strong gradient in observed continuous lattice rotations is observed, where only the near-surface region is affected. No influence of nano-lamella spacing on the depth of the affected region is observed, suggesting no pronounced effect of the nano-lamella spacing on mechanical properties.

However, an influence of grain orientation on the magnitude of lattice rotations is observed. The lattice rotation is more pronounced for grains oriented closer to <110> directions than for those growing closer to <111> directions. Considering the Schmid factors of the probable slip systems, this leads to the conclusion that mainly the $\{111\} < 1\overline{1}0 >$ and/or $\{110\} < 1\overline{1}0 >$ slip system are activated for the present wet-blasted TiAlN coatings.

CRediT authorship contribution statement

Monica Mead: Writing – original draft, Investigation, Formal analysis, Data curation. **Olof Bäcke:** Writing – review & editing, Supervision, Investigation. **Thorsten Manns:** Formal analysis. **Dirk Stiens:** Writing – review & editing, Supervision, Conceptualization. **Mats Halvarsson:** Writing – review & editing, Supervision, Funding acquisition, Conceptualization.

Declaration of Competing Interest

The authors declare the following financial interests/personal relationships which may be considered as potential competing interests:

Dirk Stiens, Thorsten Manns report financial support and equipment, drugs, or supplies were provided by Walter AG. Dirk Stiens, Thorsten Manns report a relationship with Walter AG that includes: employment. If there are other authors, they declare that they have no known competing financial interests or personal relationships that could have appeared to influence the work reported in this paper.

Acknowledgements

The work was partly financed by Vinnova, grant number 2021–04008, and the research was mainly carried out at the Chalmers Materials Analysis Laboratory (CMAL).

Monica Mead would like to acknowledge the Baden-Württemberg Stiftung, International Max Planck Research School for Condensed Matter Science (IMPRS-CMS) and Adlerbertska Foreign Student Hospitality Foundation for funding during her studies at University of Stuttgart and Chalmers University of Technology. The authors thank Emmanuelle Göthelid from Sandvik Coromant for the blast-treatment of the coated inserts.

Appendix A. Supplementary data

Supplementary data to this article can be found online at https://doi.org/10.1016/j.ijrmhm.2025.107077.

Data availability

Data will be made available on request.

References

[1] K. Bobzin, High-performance coatings for cutting tools, CIRP J. Manuf. Sci. Technol. 18 (2017) 1–9.

[2] Dedalus Consulting, N.N. Cutting Tools. 2014. https://www.dedalusconsulting.com/. (Accessed 1 February 2024).

[3] R.F. Bunshah, Handbook of Hard Coatings: Deposition Technologies, Properties and Applications, Noyes Publications; William Andrew Pub, Park Ridge, N.J., Norwich, N.Y., 2001.

[4] F. Klocke, Fertigungsverfahren 1: Zerspanung mit geometrisch bestimmter Schneide, 9th ed., Springer Berlin Heidelberg, Berlin, Heidelberg, 2018.

[5] A. Inspektor, P.A. Salvador, Architecture of PVD coatings for metalcutting applications: a review, Surf. Coat. Technol. 257 (2014) 138–153.

[6] P. Jindal, A. Santhanam, U. Schleinkofer, A. Shuster, Performance of PVD TiN, TiCN, and TiAlN coated cemented carbide tools in turning, Int. J. Refract. Met. Hard Mater. 17 (1–3) (1999) 163–170.

[7] J.H. Hsieh, A. Tan, X.T. Zeng, Oxidation and wear behaviors of Ti-based thin films, Surf. Coat. Technol. 201 (7) (2006) 4094–4098.

[8] T. Leyendecker, O. Lemmer, S. Esser, J. Ebberink, The development of the PVD coating TiAlN as a commercial coating for cutting tools, Surf. Coat. Technol. 48 (2) (1991) 175–178.

[9] M. Zhou, Y. Makino, M. Nose, K. Nogi, Phase transition and properties of Ti–Al–N thin films prepared by r.f.-plasma assisted magnetron sputtering, Thin Solid Films 339 (1–2) (1999) 203–208.

[10] M.R. Derakhshandeh, M.J. Eshraghi, M. Razavi, Recent developments in the new generation of hard coatings applied on cemented carbide cutting tools, Int. J. Refract. Met. Hard Mater. 111 (2023) 106077.

[11] R. Qiu, A. Forslund, O. Bäcke, A. Iyer, M. Sattari, W. Janssen, et al., Effects of gas flow on detailed microstructure inhomogeneities in LPCVD TiAlN nanolamella coatings, Materialia 9 (2020) 100546.

[12] I. Endler, M. Höhn, M. Herrmann, R. Pitonak, S. Ruppi, M. Schneider, et al., Novel aluminum-rich Ti1−xAlxN coatings by LPCVD, Surf. Coat. Technol. 203 (5–7) (2008) 530–533.

[13] J. Todt, J. Zalesak, R. Daniel, R. Pitonak, A. Köpf, R. Weißenbacher, et al., Al-rich cubic Al0.8Ti0.2N coating with self-organized nano-lamellar microstructure: thermal and mechanical properties, Surf. Coat. Technol. 291 (2016) 89–93.

[14] R. Qiu, O. Bäcke, D. Stiens, W. Janssen, J. Kümmel, T. Manns, et al., CVD TiAlN coatings with tunable nanolamella architectures, Surf. Coat. Technol. 413 (2021) 127076.

[15] J. Zalesak, D. Holec, I. Matko, M. Petrenec, B. Sartory, N. Koutná, et al., Peculiarity of self-assembled cubic nanolamellae in the TiN/AlN system: epitaxial self-stabilization by element deficiency/excess, Acta Mater. 131 (2017) 391–399.

[16] M. Deura, H. Sato, J. Yamaguchi, T. Hirabaru, H. Kubo, T. Momose, et al., Kinetic analysis of face-centered-cubic Ti1−Al N film deposition by chemical vapor deposition, Mater. Sci. Eng. B 264 (2021) 114992.

[17] S. Das, S. Guha, R. Ghadai, D. Kumar, B.P. Swain, Structural and mechanical properties of CVD deposited titanium aluminium nitride (TiAlN) thin films, Appl. Phys. A Mater. Sci. Process. 123 (6) (2017).

[18] M. Ben Hassine, H.-O. Andrén, A.H. Iyer, A. Lotsari, O. Bäcke, D. Stiens, et al., Growth model for high-Al containing CVD TiAlN coatings on cemented carbides using intermediate layers of TiN, Surf. Coat. Technol. 421 (2021) 127361.

[19] J. Keckes, R. Daniel, C. Mitterer, I. Matko, B. Sartory, A. Koepf, et al., Self-organized periodic soft-hard nanolamellae in polycrystalline TiAlN thin films, Thin Solid Films 545 (2013) 29–32.

[20] K. Chen, L.R. Zhao, J. Rodgers, J.S. Tse, Alloying effects on elastic properties of TiN-based nitrides, J. Phys. D. Appl. Phys. 36 (21) (2003) 2725–2729.

[21] J.O. Kim, J.D. Achenbach, P.B. Mirkarimi, M. Shinn, S.A. Barnett, Elastic constants of single-crystal transition-metal nitride films measured by line-focus acoustic microscopy, J. Appl. Phys. 72 (5) (1992) 1805–1811.

[22] W.J. Meng, G.L. Eesley, Growth and mechanical anisotropy of TiN thin films, Thin Solid Films 271 (1–2) (1995) 108–116.

[23] A.J. Wang, S.L. Shang, Y. Du, Y. Kong, L.J. Zhang, L. Chen, et al., Structural and elastic properties of cubic and hexagonal TiN and AlN from first-principles calculations, Comput. Mater. Sci. 48 (3) (2010) 705–709.

[24] A.F. Wright, Elastic properties of zinc-blende and wurtzite AlN, GaN, and InN, J. Appl. Phys. 82 (6) (1997) 2833–2839.

[25] T. Shen, L. Zhu, Z. Liu, Effect of micro-blasting on the tribological properties of TiN/MT-TiCN/Al2O3/TiCNO coatings deposited by CVD, Int. J. Refract. Met. Hard Mater. 88 (2020) 105205.

[26] M. Tkadletz, J. Keckes, N. Schalk, I. Krajinovic, M. Burghammer, C. Czettl, et al., Residual stress gradients in α-Al2O3 hard coatings determined by pencil-beam X-ray nanodiffraction: the influence of blasting media, Surf. Coat. Technol. 262 (2015) 134–140.

[27] K.-D. Bouzakis, E. Bouzakis, G. Skordaris, S. Makrimallakis, A. Tsouknidas, G. Katirtzoglou, et al., Effect of PVD films wet micro-blasting by various Al2O3 grain sizes on the wear behaviour of coated tools, Surf. Coat. Technol. 205 (2011) S128–S132.

[28] M. Gassner, N. Schalk, M. Tkadletz, C. Czettl, C. Mitterer, Thermal crack network on CVD TiCN/α-Al2O3 coated cemented carbide cutting tools, Int. J. Refract. Met. Hard Mater. 81 (2019) 1–6.

[29] Z.-Q. Zhong, L. Zhang, L. Zhou, L.-C. Qiu, H.-D. Shi, M.-L. Yang, et al., Cutting performances and the related characteristics of CVD coated hardmetal inserts changed by post-treatments, Int. J. Refract. Met. Hard Mater. 70 (2018) 162–168.

[30] C. Liu, Z. Liu, B. Wang, Modification of surface morphology to enhance tribological properties for CVD coated cutting tools through wet micro-blasting post-process, Ceram. Int. 44 (3) (2018) 3430–3439.

[31] S. Tanaka, T. Shirochi, H. Nishizawa, K. Metoki, H. Miura, H. Hara, et al., Micro-blasting effect on fracture resistance of PVD-AlTiN coated cemented carbide cutting tools, Surf. Coat. Technol. 308 (2016) 337–340.

[32] K.-D. Bouzakis, A. Tsouknidas, G. Skordaris, E. Bouzakis, Optimization of wet or dry Micro-blasting on PVD films by various Al2O3 grain sizes for improving the coated Tools' cutting performance, Tribol. Ind. 33 (2) (2011) 49–56.

[33] D. Stiens, T. Manns, S. Ruppi, TiAlCN Layers with Lamellar Structure (US10214810B2). https://patents.google.com/patent/us10214810b2/en, 2019.

[34] Carl Björmander, A Coated Cutting Tool: European Patent(EP 3 872 222). https://patentimages.storage.googleapis.com/65/19/d4/0e4a128b3fee2e/EP3872222B1.pdf, 2020 (accessed June 25, 2023).

[35] S. Gates-Rector, T. Blanton, The powder diffraction file: a quality materials characterization database, Powder Diffract. 34 (4) (2019) 352–360.

[36] A. Jain, S.P. Ong, G. Hautier, W. Chen, W.D. Richards, S. Dacek, et al., Commentary: the materials project: a materials genome approach to accelerating materials innovation, APL Mater. 1 (1) (2013).

[37] F. Bachmann, R. Hielscher, H. Schaeben, Grain detection from 2d and 3d EBSD data–specification of the MTEX algorithm, Ultramicroscopy 111 (12) (2011) 1720–1733.

[38] G. Steidl, J. Persch, R. Hielscher, R. Chan, R. Bergmann, Restoration of manifold-valued images by half-quadratic minimization, IPI 10 (2) (2016) 281–304.

[39] Evolutionary selection, a principle governing growth orientation in vapour-deposited layers, 1967.

[40] A. Forslund, A. Ruban, Surface energetics of AlxTi1-xN alloys, Comput. Mater. Sci. 183 (2020) 109813.

[41] J.A. Venables, G.D.T. Spiller, M. Hanbucken, Nucleation and growth of thin films, Rep. Prog. Phys. 47 (4) (1984) 399–459.

[42] C. Barbatti, J. Garcia, R. Pitonak, H. Pinto, A. Kostka, A. Di Prinzio, et al., Influence of micro-blasting on the microstructure and residual stresses of CVD κ-Al2O3 coatings, Surf. Coat. Technol. 203 (24) (2009) 3708–3717.

[43] J.H. Dautzenberg, J.H. Zaat, Quantitative determination of deformation by sliding wear, Wear 23 (1) (1973) 9–19.

[44] Q. Luo, W. Rainforth, W.-D. Münz, TEM studies of the wear of TiAlN/CrN superlattice coatings, Scr. Mater. 45 (4) (2001) 399–404.

[45] M. Tkadletz, A. Lechner, N. Schalk, B. Sartory, A. Stark, N. Schell, et al., Influence of spinodal decomposition and fcc→w phase transformation on global and local mechanical properties of nanolamellar CVD fcc-Ti1-xAlxN coatings, Materialia 11 (2020) 100696.

[46] R.F. Zhang, S. Veprek, Metastable phases and spinodal decomposition in Ti1−xAlxN system studied by ab initio and thermodynamic modeling, a comparison with the TiN–Si3N4 system, Mater. Sci. Eng. A 448 (1–2) (2007) 111–119.

[47] H. Cao, H. Li, F. Liu, W. Luo, F. Qi, N. Zhao, et al., Microstructure, mechanical and tribological properties of multilayer TiAl/TiAlN coatings on Al alloys by FCVA technology, Ceram. Int. 48 (4) (2022) 5476–5487.

[48] B. Zhao, X. Zhao, L. Lin, L. Zou, Effect of bias voltage on mechanical properties, milling performance and thermal crack propagation of cathodic arc ion-plated TiAlN coatings, Thin Solid Films 708 (2020) 138116.

[49] C.T. Chen, Y.C. Song, G.-P. Yu, J.-H. Huang, Microstructure and hardness of hollow cathode discharge ion-plated titanium nitride film, J. Mater. Eng. Perform. 7 (3) (1998) 324–328.

[50] J. Salamania, D.G. Sangiovanni, A. Kraych, K.M. Calamba Kwick, I.C. Schramm, L. Johnson, et al., Elucidating dislocation core structures in titanium nitride through high-resolution imaging and atomistic simulations, Mater. Des. 224 (2022) 111327.